Supporting Information for "Armoring and vertical sorting in aeolian dune fields"

Xin Gao, Clément Narteau and Olivier Rozier

Institut de Physique du Globe de Paris, Sorbonne Paris Cité, Université Paris Diderot, UMR 7154 CNRS, Paris, France

Contents of this file

1. Text S1
2. References
3. Tables S1 and S2
4. Figures S1 to S12

Corresponding author: Xin Gao (gao@ipgp.fr)

Introduction

This file contains a description of avalanching in the real-space cellular automaton dune model (Text S1, Figures S1 and S2) to explain the origin of segregation and stratification patterns in the slip face of dunes during the numerical simulations. This avalanching module has been developed according to the modeling methods proposed by *Makse et al.* [1997] and *Cizeau et al.* [1999].

Figures 3b and 4 of the main manuscript are produced by numerical simulations starting from the initial condition shown in Figure S3.

This file also contains two tables and two figures that relate the saturated sand flux ratio in the model to grain-size ratio in different natural environments (Tables S1 and S2 for subaerial and subaqueous environments, respectively; Figures S4 and S5).

Figures S6 and S7 illustrate different properties of the steady-state dune patterns discussed in the main manuscript.

Figures S8 and S9 show field examples in the Kumtagh Desert where isolated barchan dunes migrate on a coarse armor layer.

Figure S10 shows the development of isolated barchans from a flat sand bed composed at 30% of coarse particles that cannot be set in motion by the flow.

Figure S11 shows signs of abrasion by sand blasting on gravels, which indicate that the bombarding of the surface by airborne particles is the dominant process in this part of the Kumtagh Desert.

Figure S12 shows the migration of well-formed isolated barchans on a flat bed entirely composed of coarse particles that cannot be set in motion by the flow.

Text S1: Avalanches, segregation and stratification in the real-space cellular automaton dune model

To improve the sedimentary patterns associated with gravity-driven granular flows in the real-space cellular automaton dune model, *Zhang et al.* [2014] introduced a new avalanche module based on a diffusion with threshold mechanism: the threshold is simply the repose angle θ_c of the granular material; the diffusion mechanism applies to all the horizontal transitions between immobile sedimentary cells and fluid cells (see Figure 1a in *Zhang et al.* [2014]). The corresponding transition rate Λ_θ is not constant over time and depends on the local slope θ as follows

$$\Lambda_\theta = \Lambda_{\text{ava}}\delta_\theta \qquad \text{with} \qquad \delta_\theta = \begin{cases} 0 & \text{if } \theta \leq \theta_{\text{c}}, \\ 1 & \text{else.} \end{cases} \tag{1}$$

During the numerical simulations, the slope is never larger than θ_{c} when $\Lambda_{\text{ava}} \gg \Lambda_e$ (see Section 2 of the main manuscript and Table 2 of *Zhang et al.* [2014] for model parameter values).

To reduce artefacts related to the square lattice and produce realistic slip faces in the model, the slope is calculated locally using two steps. First, the slope is roughly estimated using the elevation of sedimentary cells along the principal horizontal axis at distances of $\pm 2\, l_0$ (i.e., ± 2 cells). Using the direction of this slope, we recalculate the slope at distances of $\pm k\, l_0$ using elevations which are interpolated from the four nearest neighbors. The k-value depends on the repose angle:

$$k = \begin{cases} 3.5 & \text{if } \theta_{\text{c}} \leq 33^\circ, \\ 3.0 & \text{if } 33^\circ < \theta_{\text{c}} \leq 45^\circ, \\ 1.5 & \text{else.} \end{cases}$$

Then, the transition of avalanche is randomly selected according to the local topography and the time dependent process described in Appendix B of *Narteau et al.* [2009].

Note also that the previous avalanche module is still active. When the height difference between two nearest neighbor columns of sedimentary cells is higher than a given threshold, cells from the highest columns are randomly redistributed onto the lower neighboring sites.

In the model that involves a granular binary mixture, we use two different repose angles θ^{f} and θ^{c} for fine and coarse sedimentary cells, respectively. In addition, following the model of *Makse et al.* [1997], we consider a two phase dynamic with stable and unstable phases. Finally, we end up with four repose angle: $\theta^{\mathrm{f}}_{\mathrm{s}}$ and $\theta^{\mathrm{c}}_{\mathrm{s}}$ for fine and coarse grains during the stable phase; $\theta^{\mathrm{f}}_{\mathrm{u}}$ and $\theta^{\mathrm{c}}_{\mathrm{u}}$ for fine and coarse grains during the unstable phase. The duration Δt^{s} of the stable phase is shorter than the duration Δt^{u} of the unstable one. As for model with uniform grain size, we consider a single transition rate $\Lambda_{\mathrm{ava}} \gg \Lambda_e$ for both phases.

To illustrate the behavior of avalanches in the model, we run simulations without shear flow and without the transitions associated with erosion, deposition and transport. We keep only the transition associated with the free fall of sedimentary cells, the so-called gravity, and the transitions associated with avalanches (see above and Figure 1a of *Zhang et al.* [2014]). We pour an equal-volume mixture from the top middle of the cellular space and accumulate the sedimentary cells on the ground to form a sand pile (Figure S1). The grain size, coarse or fine, of the injected sedimentary cell is randomly selected. In practice, we take $\Delta t^{\mathrm{s}} = 1000\, t_0$, $\Delta t^{\mathrm{u}} = 3.2 \times 10^4\, t_0$ and $\Lambda_{\mathrm{ava}} = 3\, t_0^{-1}$ for a circular source of grains with a radius of 5 cells. For the repose angles, we take $\theta^{\mathrm{f}}_{\mathrm{s}} = 45^\circ$, $\theta^{\mathrm{c}}_{\mathrm{s}} = 37^\circ$, $\theta^{\mathrm{f}}_{\mathrm{u}} = 37^\circ$ and $\theta^{\mathrm{c}}_{\mathrm{u}} = 33^\circ$ such that $\theta^{\mathrm{f}}_{\mathrm{u}} > \theta^{\mathrm{c}}_{\mathrm{u}} = \theta^{\mathrm{f}}_{\mathrm{s}} > \theta^{\mathrm{c}}_{\mathrm{s}}$. During an unstable phase, segregation occurs as

the coarse grains with a smaller repose angle accumulate from the external base of the sand pile (Figure S1a). At the onset of the unstable phase, fine grains quickly recover this coarse layer to create a new layer of fine sediment (Figure S1b). The repetition of these two phases lead to a stratification pattern with a wavelength which depends on the Δt^{u}-value (Figures S1c and S2).

Figure S2 shows the sand pile and the deposition patterns at two different times to demonstrate that the model reproduces the conical shape as well as stratification and segregation in 3-D. Thanks to the new avalanche module and our model, we can therefore concentrate on the slip face dynamics and sedimentary patterns in the natural dune fields.

References

Cizeau, P., H. A. Makse, and H. E. Stanley (1999), Mechanisms of granular spontaneous stratification and segregation in two-dimensional silos, *Phys. Rev. E*, *59*, 4408–4421, doi:10.1103/PhysRevE.59.4408.

Makse, H. A., S. Havlin, P. R. King, and H. E. Stanley (1997), Spontaneouos stratification in granular mixtures, *Nature*, *386*, 379–382.

Narteau, C., D. Zhang, O. Rozier, and P. Claudin (2009), Setting the length and time scales of a cellular automaton dune model from the analysis of superimposed bed forms, *J. Geophys. Res.*, *114*, F03,006, doi:10.1029/2008JF001127.

Zhang, D., X. Yang, O. Rozier, and C. Narteau (2014), Mean sediment residence time in barchan dunes, *J. Geophys. Res.*, *119*, 451–463, doi:10.1002/2013JF002833.

Table S1. Grain size ratio with respect to the saturated sand flux ratio for aeolian environments in the real-space cellular automaton dune model[a].

D_f [μm]	u [m/s]	$D_\mathrm{c}/D_\mathrm{f}$					
		$\frac{Q^\mathrm{c}_\mathrm{sat}}{Q^\mathrm{f}_\mathrm{sat}}=\frac{2}{3}$	$\frac{Q^\mathrm{c}_\mathrm{sat}}{Q^\mathrm{f}_\mathrm{sat}}=\frac{1}{2}$	$\frac{Q^\mathrm{c}_\mathrm{sat}}{Q^\mathrm{f}_\mathrm{sat}}=\frac{1}{4}$	$\frac{Q^\mathrm{c}_\mathrm{sat}}{Q^\mathrm{f}_\mathrm{sat}}=\frac{1}{8}$	$\frac{Q^\mathrm{c}_\mathrm{sat}}{Q^\mathrm{f}_\mathrm{sat}}=\frac{1}{16}$	$\frac{Q^\mathrm{c}_\mathrm{sat}}{Q^\mathrm{f}_\mathrm{sat}}=\frac{1}{32}$
168	**20**	**8.4**	**12.1**	**17.7**	**20.4**	**21.8**	**22.5**
200	15	4.3	6.0	8.5	9.7	10.3	10.7
250	10	2.0	2.4	3.2	3.5	3.7	3.8

[a]According to Equations 4 to 6 of the main manuscript, the grain size ratio can be determined from the sand flux ratio if $Q^\mathrm{f}_\mathrm{sat} > Q^\mathrm{c}_\mathrm{sat} > 0$. See the text of the main manuscript for the definition of all variables. Here we consider aeolian sand flux on Earth and we take $z = 10\,\mathrm{m}$, $z_0 = 10^{-3}\,\mathrm{m}$, $\kappa = 0.4$, $g = 9.81\ \mathrm{m/s^{-2}}$, $\rho_\mathrm{s} = 2.55 \times 10^3\ \mathrm{kg/m^3}$ and $\rho_\mathrm{f} = 1.29\ \mathrm{kg/m^3}$. Arbitrarily, we used the values shown in bold in the main manuscript.

Table S2. Grain size ratio with respect to the saturated sand flux ratio for subaqueous environments in the real-space cellular automaton dune model[b].

D_f [μm]	u [m/s]	$D_\mathrm{c}/D_\mathrm{f}$					
		$\frac{Q^\mathrm{c}_\mathrm{sat}}{Q^\mathrm{f}_\mathrm{sat}}=\frac{2}{3}$	$\frac{Q^\mathrm{c}_\mathrm{sat}}{Q^\mathrm{f}_\mathrm{sat}}=\frac{1}{2}$	$\frac{Q^\mathrm{c}_\mathrm{sat}}{Q^\mathrm{f}_\mathrm{sat}}=\frac{1}{4}$	$\frac{Q^\mathrm{c}_\mathrm{sat}}{Q^\mathrm{f}_\mathrm{sat}}=\frac{1}{8}$	$\frac{Q^\mathrm{c}_\mathrm{sat}}{Q^\mathrm{f}_\mathrm{sat}}=\frac{1}{16}$	$\frac{Q^\mathrm{c}_\mathrm{sat}}{Q^\mathrm{f}_\mathrm{sat}}=\frac{1}{32}$
168	0.6	10.2	14.9	21.8	25.3	27.0	27.9
200	0.4	4.2	5.9	8.3	9.5	10.1	10.4
250	0.2	1.4	1.6	1.9	2.0	2.1	2.2

[b]According to Equations 4 to 6 of the main manuscript, the grain size ratio can be determined from the sand flux ratio if $Q^\mathrm{f}_\mathrm{sat} > Q^\mathrm{c}_\mathrm{sat} > 0$. See the text of the main manuscript for the definition of all variables. Here we consider subaqueous sand flux on Earth and we take $z = 1\,\mathrm{m}$, $z_0 = 10^{-3}\,\mathrm{m}$, $\kappa = 0.4$, $g = 9.81\ \mathrm{m/s^{-2}}$, $\rho_\mathrm{s} = 2.55\times10^3\ \mathrm{kg/m^3}$ and $\rho_\mathrm{f} = 10^3\ \mathrm{kg/m^3}$.

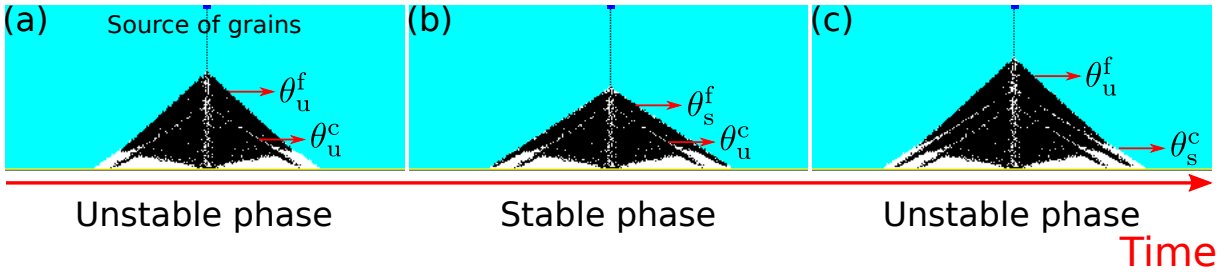

Figure S1. Time sequence of the sediment layers produced by avalanching in the real-space cellular automaton dune model with two grain sizes. Fine and coarse sedimentary cells are shown in black and white, respectively. We pour an equal-volume mixture in the middle-top of the cellular space (blue box). Different repose angles $\theta^{\{f,c\}}_{\{u,s\}}$ and model parameters are described in Text S1. Each figure shows the same vertical slice of cells. Note the patterns of segregation and stratification as well as the accumulation of coarse grains at the base of the sand pile.

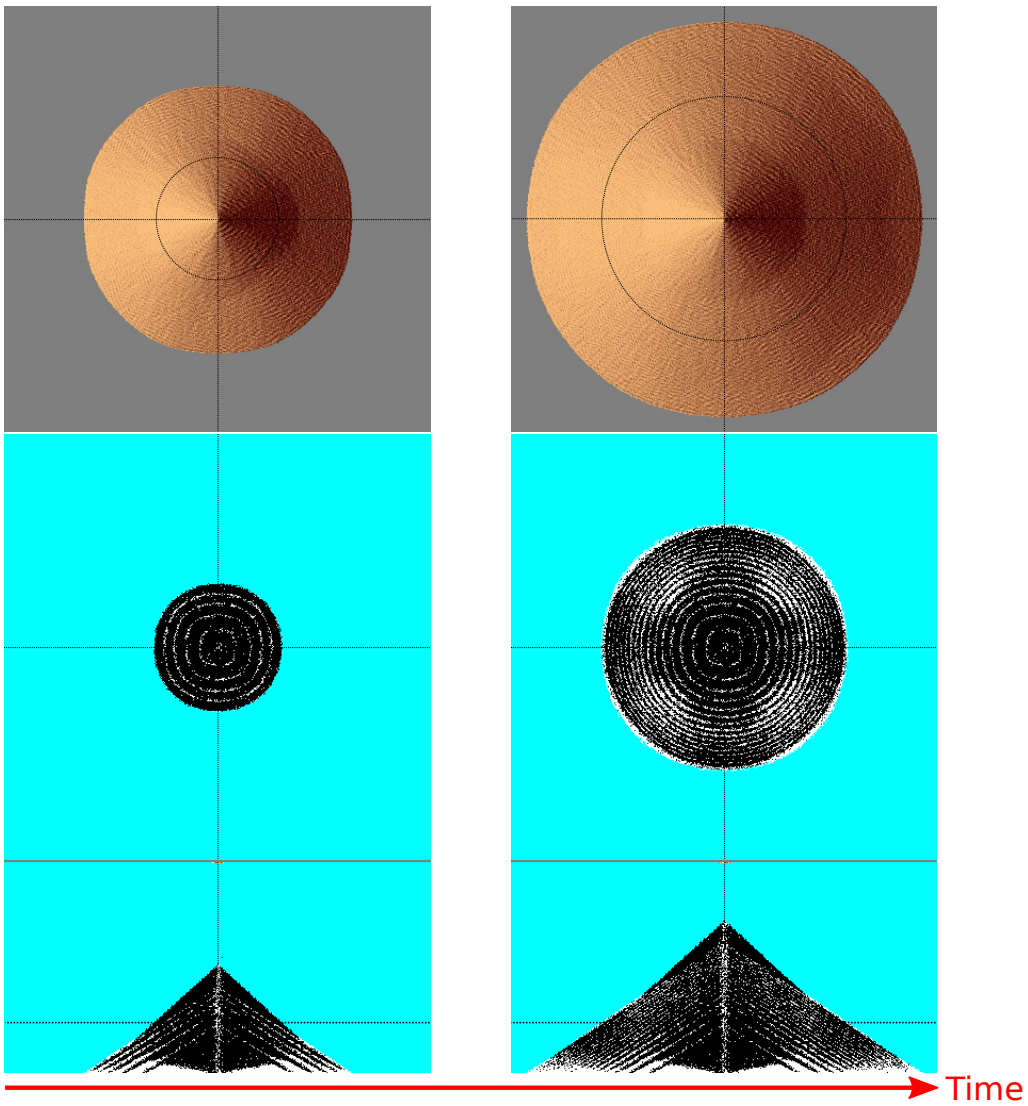

Figure S2. The sand pile and the sediment layers produced by avalanching in the real-space cellular automaton dune model with two grain sizes. From top to bottom, the figure shows a top view of the sand pile, a vertical slice of cells and a horizontal one. Fine and coarse sedimentary cells are shown in black and white, respectively. In each figure, the black lines show the slices of cells displayed in the other figures. Note the patterns of segregation and stratification as well as the accumulation of coarse grains at the base of the sand pile. As shown by the conical shape of the sand pile and the radial symmetry of the segregation and stratification patterns, the procedure explained in the Text S1 limits the artefacts related to the square lattice.

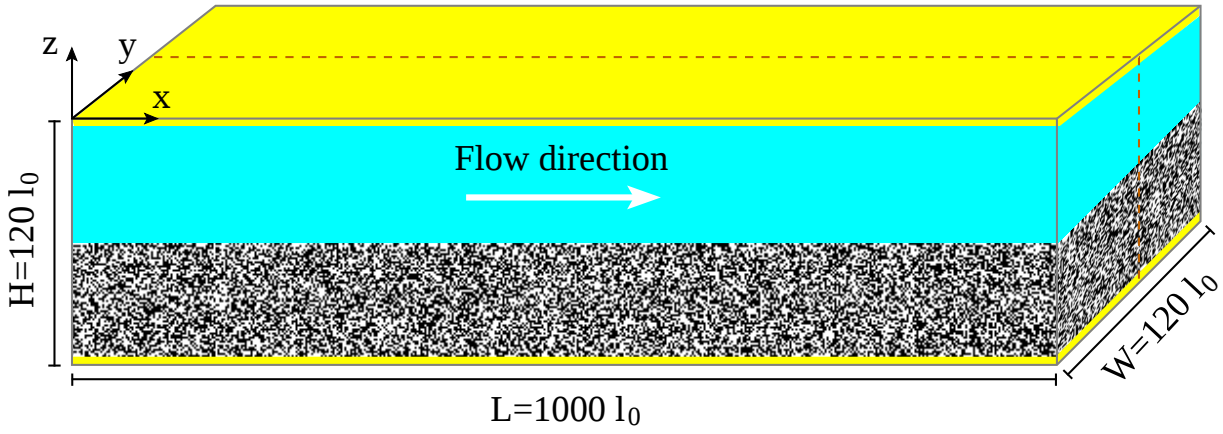

Figure S3. Initial condition and dimensions of the cellular space. Fine and coarse sedimentary cells are shown in black and white, respectively. Neutral cells of the solid bedrock and the ceiling are shown in yellow. Fluid cells are shown in cyan.

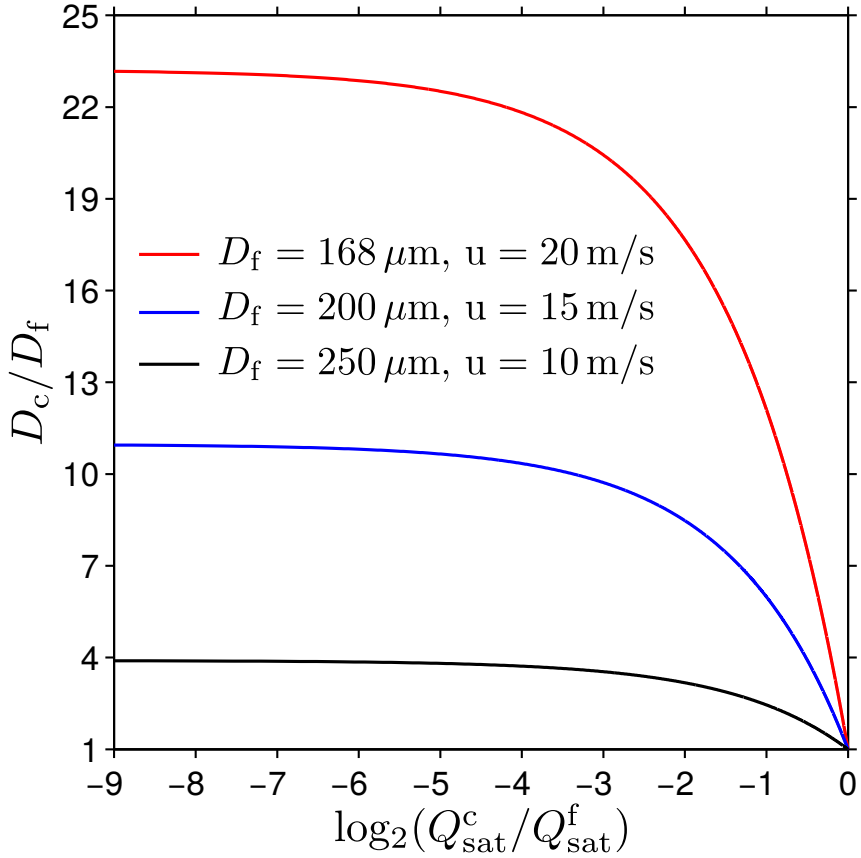

Figure S4. The grain size ratio D_c/D_f with respect to the saturated sand flux ratio Q^c_{sat}/Q^f_{sat} in aeolian environments for different fine grain sizes D_f and wind speeds u at a height z of 10 m (see Equations 4 to 6 of the main manuscript and Table S1 for the model parameter values).

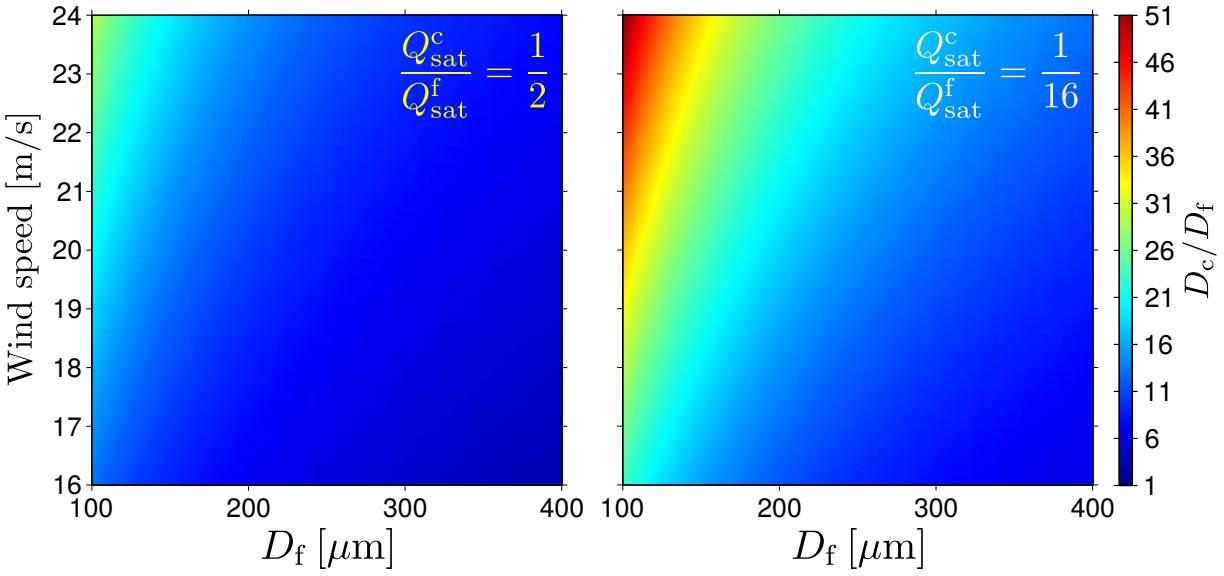

Figure S5. Grain size ratio D_c/D_f in aeolian environment with respect to fine grain diameter D_f and wind speed u at a height z of 10 m (see Equations 4 to 6 of the main manuscript and Table S1 for the model parameter values).

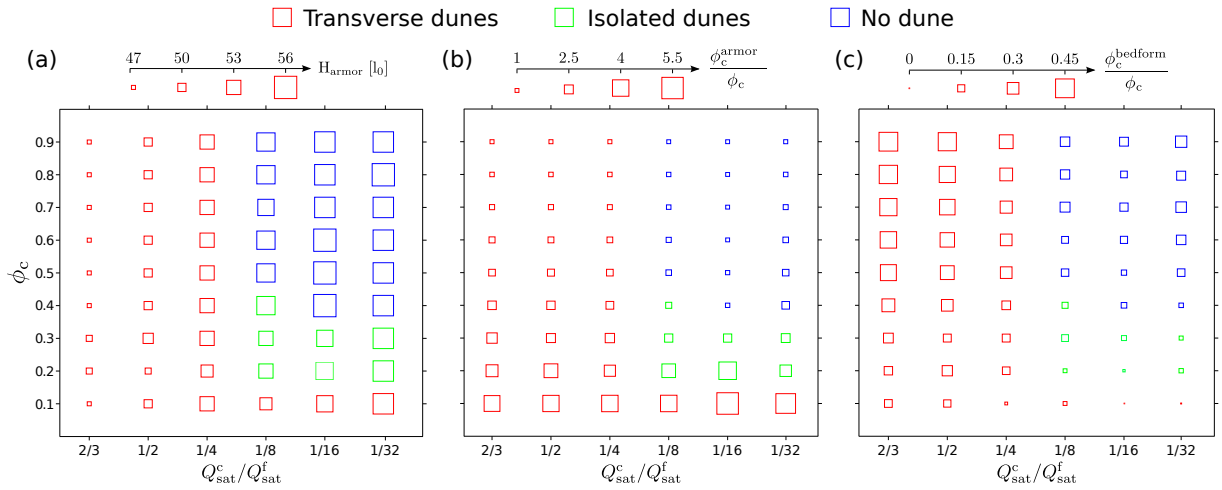

Figure S6. Properties of steady-state dune fields in the $\{\phi_c, Q_{sat}^c/Q_{sat}^f\}$ parameter space. (a) The height of armor layers H_{armor}. In all cases, the initial flat bed has a height of $60\,l_0$. (b) Relative increase of the proportion of coarse grains within the armor layer with respect to the initial proportion of coarse grains (i.e., $\phi_c^{armor}/\phi_c > 1$). (c) Relative decrease of the proportion of coarse grains within bed forms with respect to the initial proportion of coarse grains (i.e., $\phi_c^{bedform}/\phi_c < 1$).

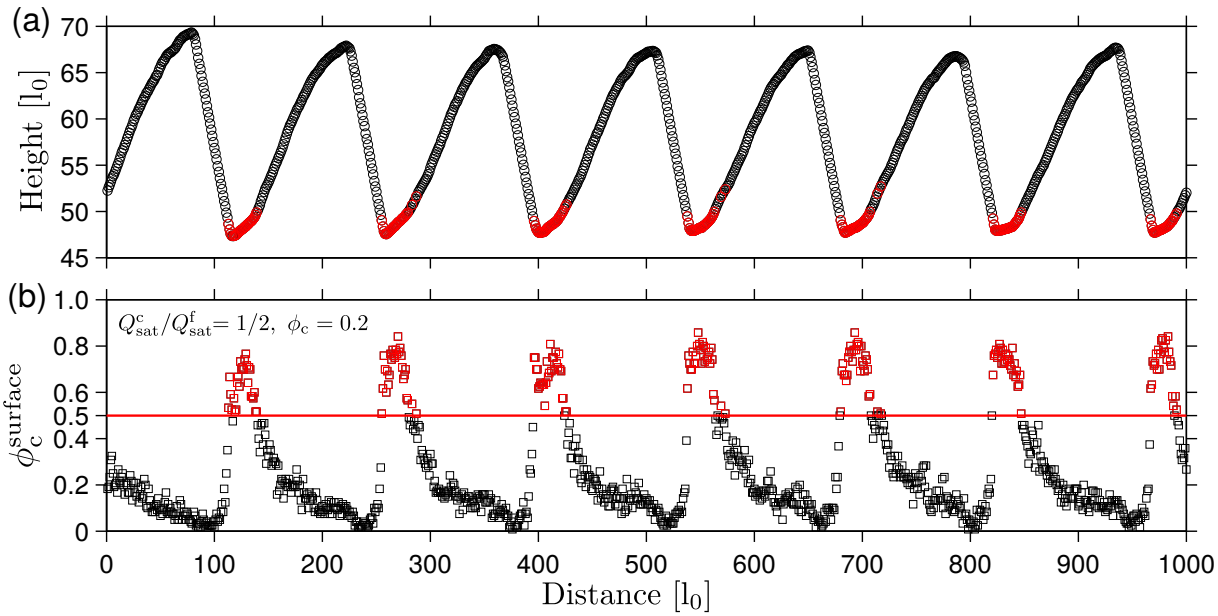

Figure S7. Distribution of coarse grains on the bed surface in a steady-state transverse dune field with $\phi_c = 0.2$ and $Q^{c}_{sat}/Q^{f}_{sat} = 1/2$. (a) The bed elevation profile of a vertical cross-section parallel to the direction of the flow. (b) The proportion of coarse grains on the surface $\phi_c^{surface}$ along the same cross-section. Parts where $\phi_c^{surface} > 0.5$ are shown in red in (a) and (b). Note that the proportion of coarse grains is the highest in troughs where the mobile armor layer is observed. The proportion of coarse grains systematically decreases with height at the surface of dunes.

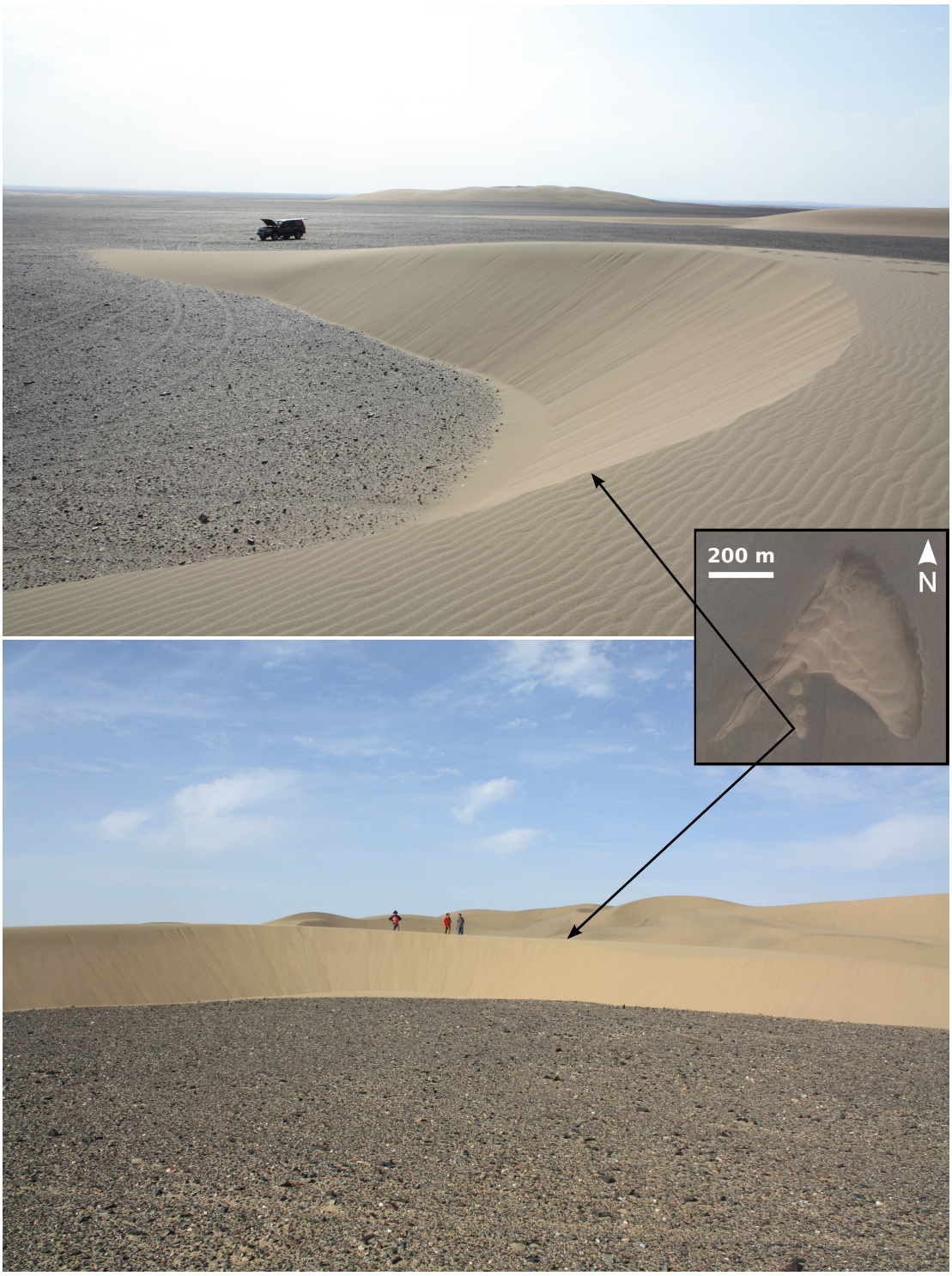

Figure S8. Dunes, armor and vertical sorting in the Kumtagh Desert, Northwest China (40°35′ N, 92°59′ E). Pictures were taken during a field trip in August 2011. Coarse grains are darker than fine grains. Note the clear transition from the coarse grains of the armor layer to the fine grains of the barchan dune.

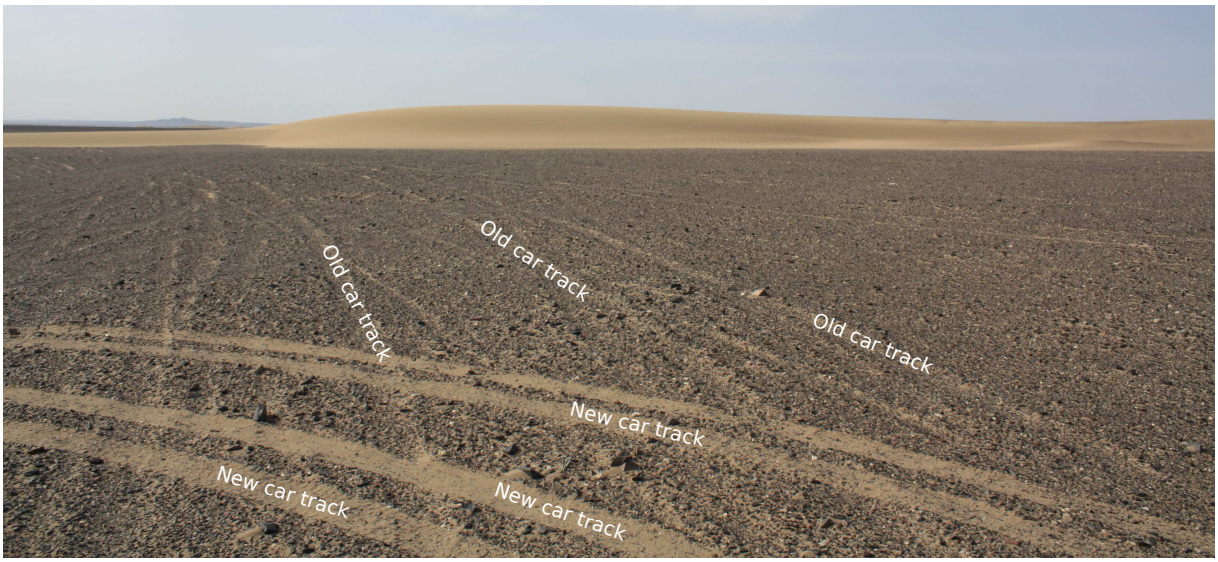

Figure S9. Surface and subsurface sedimentary layers in the Kumtagh Desert, Northwest China (40°35′ N, 92°59′ E). The picture was taken during a field trip in August 2011. Coarse grains are darker than fine grains. Note that the pressure imposed by car wheels causes the coarse grains to penetrate deep into the underlying sediments which have a much smaller and uniform density of coarse grains. As the dynamical armoring is always active, one can distinguish between new and old car tracks.

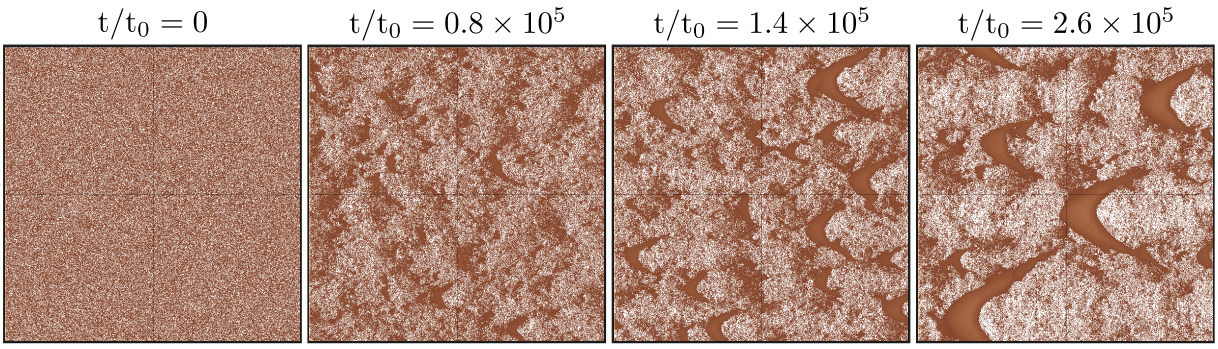

Figure S10. Development of isolated barchans from a flat sand bed composed at 30% of coarse particles that cannot be set in motion by the flow: $\phi_c = 0.3$ and $Q^c_{sat}/Q^f_{sat} \to 0$ (i.e., $D_c \to \infty$ for D_f-values shown in Table S1). Coarse sedimentary cells are shown in white.

Figure S11. Signs of abrasion by sand blasting on gravels, which indicate that the bombarding of the surface by airborne particles is the dominant process in this part of the Kumtagh Desert.

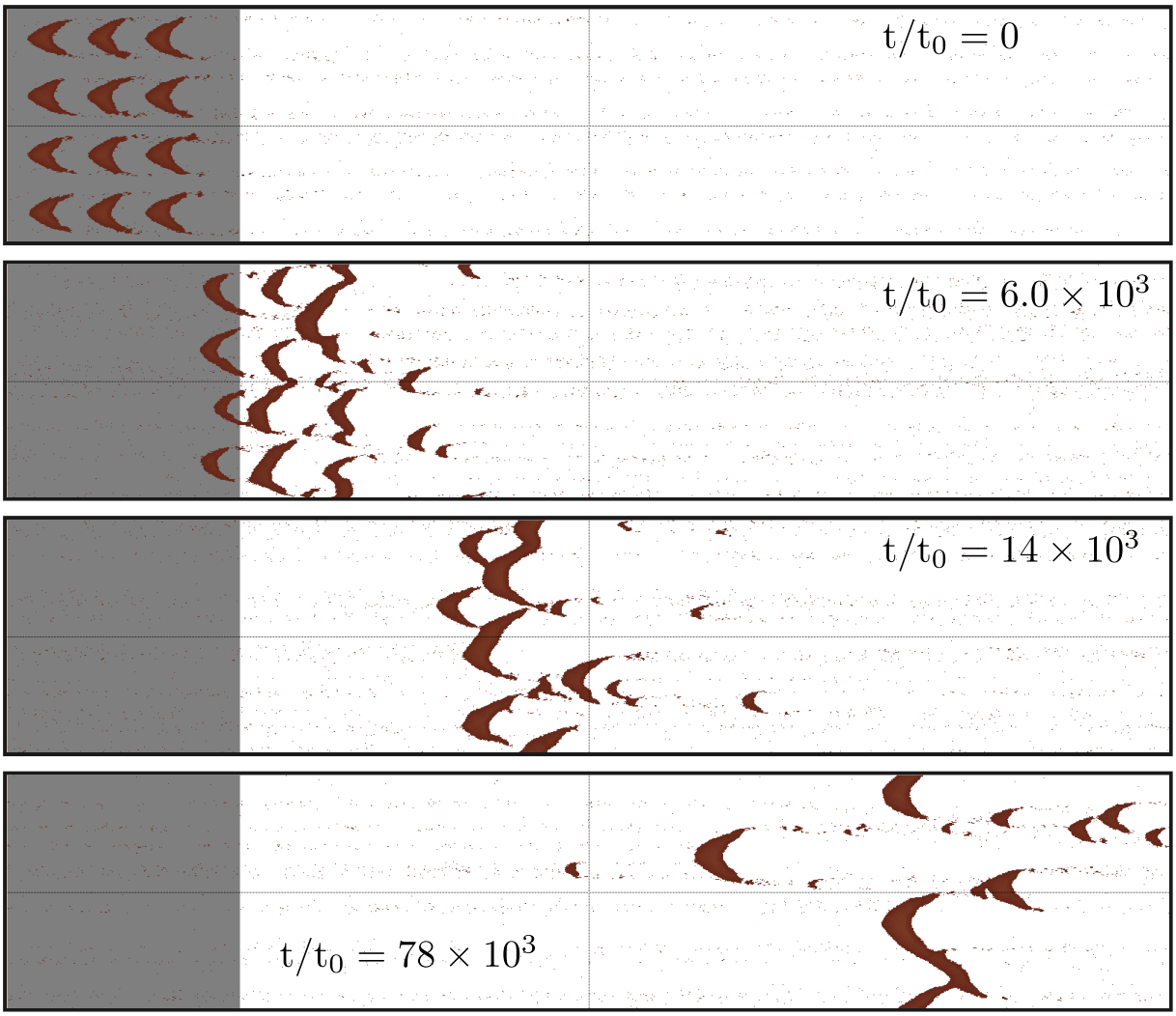

Figure S12. Migration of well-formed isolated barchans on a flat bed entirely composed of coarse particles that cannot be set in motion by the flow (i.e., $D_c \to \infty$ for D_f-values shown in Table S1). The bedrock is shown in grey. Coarse sedimentary cells are shown in white.